MOLECULAR IMAGING AND BIOLOGY

Published Online: 8 September 2010

Mol Imaging Biol (2011) 13:973–984
DOI: 10.1007/s11307-010-0406-x

RESEARCH ARTICLE

Pancreatic Beta Cell Mass PET Imaging and Quantification with [^{11}C]DTBZ and [^{18}F]FP-(+)-DTBZ in Rodent Models of Diabetes

Tarun Singhal,[1] Yu-Shin Ding,[1] David Weinzimmer,[1] Marc D. Normandin,[1] David Labaree,[1] Jim Ropchan,[1] Nabeel Nabulsi,[1] Shu-fei Lin,[1] Marc B. Skaddan,[3] Walter C. Soeller,[3] Yiyun Huang,[1] Richard E. Carson,[1] Judith L. Treadway,[3] Gary W. Cline[2]

[1]*Department of Diagnostic Radiology, Yale University School of Medicine, New Haven, CT, USA*
[2]*Department of Internal Medicine, Yale University School of Medicine, P. O. Box 208020, New Haven, CT 06520-8020, USA*
[3]*Pfizer Global R&D, Groton, CT, USA*

Abstract

Purpose: The aim of this study is to compare the utility of two positron emission tomography (PET) imaging ligands ((+)-[^{11}C]dihydrotetrabenazine ([^{11}C]DTBZ) and the fluoropropyl analog ([^{18}F]FP-(+)-DTBZ)) that target islet β-cell vesicular monoamine transporter type II to measure pancreatic β-cell mass (BCM).

Procedures: [^{11}C]DTBZ or [^{18}F]FP-(+)-DTBZ was injected, and serial PET images were acquired in rat models of diabetes (streptozotocin-treated and Zucker diabetic fatty) and β-cell compensation (Zucker fatty). Radiotracer standardized uptake values (SUV) were correlated to pancreas insulin content measured biochemically and histomorphometrically.

Results: On a group level, a positive correlation of [^{11}C]DTBZ pancreatic SUV with pancreas insulin content and BCM was observed. In the STZ diabetic model, both [^{18}F]FP-(+)-DTBZ and [^{11}C]DTBZ correlated positively with BCM, although only ~25% of uptake could be attributed to β-cell uptake. [^{18}F]FP-(+)-DTBZ displacement studies indicate that there is a substantial fraction of specific binding that is not to pancreatic islet β cells.

Conclusions: PET imaging with [^{18}F]FP-(+)-DTBZ provides a noninvasive means to quantify insulin-positive BCM and may prove valuable as a diagnostic tool in assessing treatments to maintain or restore BCM.

Key words: Imaging, Pancreas, Islet, Beta-cell mass, PET, VMAT2

Introduction

Pancreatic islet β cells, representing ~2% of pancreatic mass, synthesize and release insulin to maintain normoglycemia. Alterations in the structural and functional integrity of the β cells are implicated in disorders like diabetes mellitus, insulinoma, and nesidioblastosis. Diabetes is a widespread health disorder having a prevalence of up to 10% of the general population in some countries. Type 1 diabetes is characterized by autoimmune destruction of β-cell mass (BCM), typically in young individuals. Type 2 diabetes, on the other hand, is characterized by peripheral insulin resistance, insulin overproduction, β-cell hyperplasia followed by β-cell failure, and loss of BCM resulting in insufficient insulin production and hyperglycemia.

Correspondence to: Gary W. Cline; *e-mail:* gary.cline@yale.edu

With the growing research on beta-cell transplantation and availability of drugs that lead to a preservation of functional β-cell mass in diabetic patients [1], there has been a growing interest in the development of noninvasive measures of BCM [2, 3]. Metabolic measurements like acute insulin responses to intravenous arginine or glucose, the intravenous arginine stimulation test, or oral and intravenous glucose tolerance tests have been used to provide an indirect estimate of BCM. Although these tests have shown good correlation with histomorphometric measurements of BCM, each has its own limitations [4, 5]. Over the last several years, considerable progress has been made by several groups to accomplish the goal of *in vivo* imaging of β-cell mass. These include magnetic resonance imaging using contrast agents such as iron-oxide particles [6], and recently, promising results were reported that exploit the increased uptake of manganese into β cells through voltage-gated calcium channels in response to glucose stimulus [7]. Alternatively, positron emission tomography (PET)-based approaches have employed radioligands that target receptor binding sites enriched in pancreatic islets (*i.e.*, sulfonylurea receptors and other binding sites) [8–11]. Of the radioligands identified to date, those targeting vesicular monoamine transporter type II (VMAT2) have shown the most promise [12–17].

VMAT2 is responsible for the storage and release of monoamines such as dopamine, norepinephrine, and serotonin in the transport vesicles of synaptic terminals of monoaminergic neurons [18]. VMAT2 alterations in the brain have been conventionally studied using (+)-^{11}C-dihydrotetrabenazine ([^{11}C]DTBZ) in Parkinson's disease [19]. The distribution of VMAT2 in the whole body has been described in detail [18]. In addition, VMAT2 has been found to be coexpressed in pancreatic beta cells along with insulin [19–21]. This expression of VMAT2 is specific to beta cells among the islet cells [19, 20]. Although the exact function of VMAT2 in pancreatic beta cells is not known, concomitant release of dopamine may play a role in insulin release [14]. PET imaging studies in two rat models of type 1 diabetes (*i.e.*, streptozotocin (STZ) induced diabetes and the BioBreeding diabetes-prone (BB-DP) rats) using [^{11}C]DTBZ showed proportional reductions in pancreatic binding in concert with reductions of BCM [15, 16]. A recent PET imaging study in humans has shown a correlative reduction in total [^{11}C]DTBZ binding in the pancreas in type 1 diabetic patients as compared to healthy controls [17]. These results are promising and suggest that [^{11}C]DTBZ may be a useful PET imaging agent to determine reductions in β-cell mass in type 1 diabetic patients. However, it is unclear whether [^{11}C]DTBZ is able to quantify BCM as compensatory expansion followed by β-cell failure occurs during the progression from insulin resistance to type 2 diabetes. Functional and morphological changes in islets that occur during the development of type 2 diabetes may impact VMAT2 content and, hence, quantitative PET imaging of DTBZ binding. The first aim of this study was to evaluate whether [^{11}C]DTBZ uptake quantitatively correlates with compensatory β-cell hyperplasia associated with obesity-induced insulin resistance in the Zucker fatty (ZF) rat and during the progression to type 2 diabetes in the Zucker diabetic fatty (ZDF) rat.

Recently, an ^{18}F-labeled fluoropropyl derivative of DTBZ, [^{18}F]FP-(+)-DTBZ ([^{18}F]FP-(+)-DTBZ, or ^{18}F-AV-133 (Avid Radiopharmaceuticals, Philadelphia, PA, USA), the active enantiomer of [^{18}F]FP-(±)-DTBZ), has been developed with the advantage of an improved binding affinity to VMAT2 compared to [^{11}C]DTBZ (K_i values for [^{18}F]FP-(+)-DTBZ and [^{11}C]DTBZ are 0.1 and 0.97 nM, respectively) [22]. In earlier studies, significant background binding of [^{11}C]DTBZ compromised its use to detect modest changes in BCM, thereby limiting its use as a diagnostic tool to evaluate the effectiveness of therapies designed to prevent loss of or restore BCM. Whether the increased binding affinity of [^{18}F]FP-(+)-DTBZ translates to improved ability to quantify islet BCM from the exocrine pancreas is yet to be shown. Therefore, the second aim of this study was to compare the utility of these two VMAT2-targeted PET imaging ligands, [^{11}C]DTBZ and [^{18}F]FP-(+)-DTBZ, to measure BCM in rats with variable degrees of STZ-induced beta-cell loss as a model of the progression of type 1 diabetes.

Materials and Methods

Radiochemistry

[^{11}C]DTBZ was synthesized at the Yale University School of Medicine PET Center following established protocols as previously described [23].

Radioisotope C-11 carbon dioxide ([^{11}C]CO_2) was produced by the ^{14}N(p,α)^{11}C nuclear reaction with the PETtrace cyclotron (GE Medical Systems) using 16.5±0.1 MeV proton irradiation (40 min, 55 μA) of nitrogen gas containing 0.5% oxygen. C-11 methyl iodide ([^{11}C]CH_3I) was synthesized from [^{11}C]CO_2 using a GE MeI Microlab®. Briefly, [^{11}C]CO_2 was reduced by hydrogen with a Ni catalyst to C-11 methane ([^{11}C]CH_4) followed by a gas phase reaction with iodine to form [^{11}C]CH_3I [24], which was then delivered to the GE TRACERlab FxC automated synthesis module for incorporation.

A solution of 0.51 mg (1.67 μmol) of (+)9-*O*-desmethyl-α-dihydrotetrabenazine in 300 μL of anhydrous DMF was vortexed for 1 min. Just prior to delivery of CO_2 to the MicroLab, 1.7 μL of a 1-N KOH solution was added and the mixture was vortexed for an additional minute. [^{11}C]CH_3I (generated from the MicroLab) was transferred to the FXc module and converted via a silver triflate oven preheated at 190°C to [^{11}C]MeOTf [25], which was then bubbled into the above solution of precursor at −20°C. Reaction was allowed to occur for 4 min at 75°C. The reaction was cooled to 65°C, diluted with deionized (DI) water (1.0 mL) and loaded onto a semipreparative high-performance liquid chromatography (HPLC) column (Prodigy ODS (3) 10 μm 10×250 mm). The column was eluted under isocratic conditions with a mobile phase composed of 80:20 (*v*/*v*) 0.1 N ammonium formate–acetic acid buffer pH 4.2/

CH_3CN at a flow rate of 5 mL/min. The product peak at 12.5–13 min was collected, diluted with DI water (50 mL), and loaded onto a pre-conditioned Waters Classic C18 SepPak. The SepPak was rinsed with 0.001 N HCl (10 mL), and the product was eluted with ethanol (1 mL), followed by USP saline (3 mL) into the FxC's intermediate product vessel. The resulting solution was then passed through a sterile 0.2-mm membrane filter (13 mm, 8 Millipore MILLEX GV) into a sterile assembly comprised of a 1-mL empty vial connected to a vented 10-mL dose vial containing a mixture of 7 mL saline (USP, American Regent) and 40 μL of 4.2% sodium bicarbonate (Abraxis, sterile, preservative and pyrogen-free).

The final product was analyzed by HPLC for its quality. A Shimadzu LC-20AT Prominence system was used, which is equipped with a SPD-M20A Diode Array (PDA) detector or SPD-20A UV/Vis detector (254 nm) operating in series with a Bioscan Flow-Count γ-detector. Quality control analysis was performed by using an analytical column (Phenomenex Luna C18(2) 5 μm 4.6×250 mm) eluting with 0.1 N ammonium formate–acetic acid buffer pH 4.2/CH_3CN (80/20 *v*/*v*) at a flow rate of 2 min/min. The specific activity for [^{11}C]DTBZ was determined by counting an aliquot of the product solution in a dose calibrator for the radioactivity amount and determining the mass by HPLC against a calibration curve relative mass to UV area of the reference standard (DTBZ). Product identity was confirmed by a coinjection of the product with the reference standard onto the analytical HPLC and observation of the co-elution.

[^{18}F]FP-(+)-DTBZ, (2*R*,3*R*,11b*R*)-[^{18}F]9-(3-fluoropropoxy)-3-isobutyl-10-methoxy-2,3,4,6,7,11b-hexahydro-1*H*-pyrido[2,1-*a*] isoquinolin-2-ol, was obtained from Avid Radiopharmaceuticals, Inc.

Animals

All animal studies were reviewed and approved by the Institutional Animal Care and Use Committee. Imaging sessions to determine pancreatic [^{11}C]DTBZ imaging studies were performed in three rat models that were expected to represent an ~10-fold range of islet BCM [1, 26, 27]. The ZF rats (age 8, 12, 16 weeks, n=5 each) adapt with ~4-fold increase in BCM, whereas BCM decreases in the ZDF rats (age 8, 12, 16 weeks, n=4 to 6 each) with age. In our third model (S-D rats, age 10 weeks), BCM was determined in healthy controls (n=6) and in a second group, 5 days (120 h) after β-cell death was chemically induced with streptozotocin (65 mg in sterile saline per kilogram, intraperitoneal, n=5 each). [^{18}F]FP-(+)-DTBZ imaging studies were performed in two cohorts: S-D rats (age 10 weeks), before (n=9) and 13–96 h after treatment with STZ (n=15).

PET Scanning

Immediately prior to the PET scan, rats were anesthetized using a RC2 Rodent Circuit manufactured by VetEquip with 2.5% isoflurane and placed in temperature-regulated plexiglass cylinder equipped to maintain the rat under isoflurane anesthesia with access to the tail for catheter placement. The aperture of the high-resolution research tomograph (HRRT) scanner was equipped with a custom-built insert to hold three cylinders symmetrically spaced for simultaneous imaging of three rats during each session. The animals were positioned so that the tail was outside the axial field-of-view of the scanner.

For each rat, a 25-G butterfly catheter was placed in the tail vein and kept patent with a 10% heparin saline flush. Approximately 12–28 MBq of [^{11}C]DTBZ or [^{18}F]FP-(+)-DTBZ in 200 μL was injected in the tail vein, and list mode events were acquired over 120 min for [^{11}C]DTBZ, or 180 min for [^{18}F]FP-(+)-DTBZ, using the HRRT (Siemens Medical Systems). In some sessions (n=16), a bolus injection of unlabeled FP-(+)-DTBZ (2.5 mg/kg) was given 90 min following the injection of [^{18}F]FP-(+)-DTBZ to displace specific binding and to ascertain the magnitude of nonspecific binding to the pancreas. In a different set of rats (n=3), the fraction of parent compound, [^{18}F]FP-(+)-DTBZ, and its metabolites were determined by HPLC analysis of plasma, pancreas, liver, and kidney at 60, 90, and 120 min after tracer injection.

PET images were reconstructed with a cluster-based list mode OSEM algorithm (2 iterations, 30 subsets) with corrections for attenuation, randoms, scatter, and deadtime [28]. The final reconstructed images cover 207 slices, with 256×256 pixels per slice, with a pixel size of 1.2 mm. Resolution (full width at half maximum) is 2–3 mm. Summed images over the first 10 min of scanning were used for defining pancreatic regions of interest (ROI) based on an area of increased radiotracer accumulation on transverse images lying anterior to and between the two kidneys, posterior to the stomach, and below the liver. The landmark organs of liver, kidney, and stomach were anatomically identifiable from the images, and the ROIs were manually placed across the image planes. To prevent subjective biases in quantifying pancreatic BCM in the PET image, all ROIs were assigned blinded with respect to the rat strain, prior STZ treatment, insulin content, or immunohistochemistry (IHC)-determined BCM.

Data Analysis

Time–activity curves (TACs) of radiotracer normalized to body weight and injected dose (SUV, see below) were plotted from the assigned ROIs. Pancreatic SUV and the ratio of pancreas to liver (P/L) SUVs were evaluated for quantification of BCM. The time period of 60–90 min postinjection was used for SUV and P/L calculation.

Pancreatic Standardized Uptake Value

Concentrations of radioactivity within the pancreatic ROI were expressed as dimensionless SUV, defined as [tissue activity concentration (MBq/g)×body weight (g)/injected dose (MBq)]. Similarly, hepatic, gastric, and renal SUVs were calculated. Injected dose was assayed from the total activity in the rat computed by summing all pixel values from the PET images.

Nonspecific and Specific Pancreatic Binding of [^{18}F]FP-(+)-DTBZ in Control and Diabetic Rats

The fraction of specific and nonspecific binding was determined in a subgroup of rats that received a bolus injection of 2.5 mg/kg

unlabeled FP-(+)-DTBZ 90 min after the initial injection of [^{18}F]FP-(+)-DTBZ. Total binding is the sum of the specific and nonspecific binding and was calculated as the average SUV from 60 to 90 min following injection of [^{18}F]FP-(+)-DTBZ. Nonspecific binding was calculated as the average SUV remaining 60–90 min after the bolus injection of unlabeled FP-(+)-DTBZ. Specific binding was assumed to be equivalent to the readily displaceable activity and was calculated as the difference in SUV before (*i.e.*, total binding) and after (*i.e.*, nonspecific binding) the bolus of unlabeled FP-(+)-DTBZ.

Insulin Content and Fractional Islet Area

Animals from each group imaged with [^{11}C]DTBZ were divided randomly for quantification of either pancreas insulin content or for pancreatic islet area. For the animals imaged with [^{18}F]FP-(+)-DTBZ, the excised pancreas was divided into three sections for assays of radioactivity, insulin content, and islet area.

Pancreas Insulin Content

Following the imaging session, select animals were euthanized and the pancreas was excised, weighed, and placed in acid–ethanol (75% ethanol with 1.5% HCl) overnight (twice) to extract total insulin. The extracts were combined and centrifuged (13,000 rpm, 5 min, 4°C) and the supernatant assayed for insulin content by radioimmunoassay (Linco, St. Louis, MO, USA).

Quantification of Pancreatic Islet Area

Within 2 days of the [^{11}C]DTBZ imaging sessions, in select animals, the pancreas was fixed for histomorphometric and immunohistochemical analysis of pancreatic islet area. While maintained under isoflurane anesthesia, an 18-gauge needle was inserted into the left ventricle of the heart, and the posterior vena cava was cut. The rats were then perfused with ice-cold PBS until no more blood was visible, followed by a perfusion of 4% paraformaldehyde. The pancreas was removed and fixed in 4% paraformaldehyde solution overnight with gentle shaking, dewaxed, rehydrated, and embedded in paraffin. Alternatively, for the [^{18}F]FP-(+)-DTBZ studies, the pancreas was excised immediately following the imaging session, and one third of the pancreas was embedded and frozen in media (Neg −50, Richard-Allan Scientific Inc, Kalamazoo, MI, USA) and stored at −80°C until cryosectioned and stained.

Slides with 5-μm slices of the embedded pancreas were prepared with a Leica CM1850 cryotome and stained with hematoxylin and eosin (H&E) to visualize the islet area. Alternating slides of each pancreas section were stained with guinea pig anti-insulin antibody (Zymed Laboratories, San Francisco, CA, USA) and visualized with fluorescein-conjugated goat anti-guinea pig IgG (Jackson ImmunoResearch Laboratories, Inc., West Grove, PA, USA). The fraction of the islet area in the pancreas was determined from the digital image acquired using Zeiss Axioskop 40/Axiocam light microscope and quantified using ImageJ [29]. The islets were clearly distinguishable by H&E by stain contrast and architecture. Percent islet area was calculated from the integrated islet area to total pancreas area. Insulin-positive islet area was calculated from the product of the normalized fluorescence intensity of anti-insulin-positive islets, determined by IHC, and the total islet area determined by H&E staining.

Statistical Analysis

Differences between groups were analyzed using a two-sample *t* test. Correlation between mean pancreatic SUV or P/L ratio *vs*. mean insulin content and mean percent beta-cell area for each group was explored using Pearson's coefficient. Similarly, correlations between hepatic, gastric, and renal SUVs and reference pancreatic indices were explored. A dual tail probability of <5% was considered statistically significant.

Results

Radiotracers

Quality control (QC) analysis with HPLC showed the product [^{11}C]DTBZ to have >96% chemical purity and >99% radiochemical purity. The average radiochemical yield (n=12) was 100±45 mCi corresponding to a radiochemical yield of 12.0±4.6% based on trapped [C-11]MeOTf (not corrected for decay). The average specific activity of [^{11}C]DTBZ was 11.3±3.5 mCi/nmol at the time of QC after radiosynthesis.

QC analysis showed the product [^{18}F]FP-(+)-DTBZ to have >99% radiochemical purity and an average specific activity of 3.7±0.6 mCi/nmol at the time of QC after radiosynthesis.

PET Imaging

Representative transverse abdominal images of control and STZ-induced diabetic S-D rats following injection of [^{11}C]DTBZ are shown in Fig. 1a–d. For orientation, Fig. 1e is a representative sagittal image of a healthy S-D rat following injection of [^{18}F]FP-(+)-DTBZ. In the summed images of the first 10 min postinjection (Fig. 1a, b), the radiotracer intensity is dominated by tracer delivery, visualizing high-flow organs (primarily the kidney cortex, liver, and the pancreas), whereas the later images are summed from 60 to 90 min (Fig. 1c, d) and represent specific and nonspecific binding of the radiotracer by the kidney, liver, pancreas, and stomach. In these axial views, the kidney cortex is not in view, but is clearly visible in slices inferior to those shown in Fig. 1.

Tissue Time–Activity Curves

The mean TACs, expressed as SUV, observed in the control S-D rats for both [^{11}C]DTBZ (Fig. 2a) and [^{18}F]FP-(+)-DTBZ (Fig. 2b) were very similar. Immediately after bolus injection, there was a sharp rise followed by a rapid decline within 15 min of activity observed in the kidney cortex. The dynamics of the TACs for the pancreas and liver both showed a rapid rise to reach a plateau within ~15 min. In contrast, the

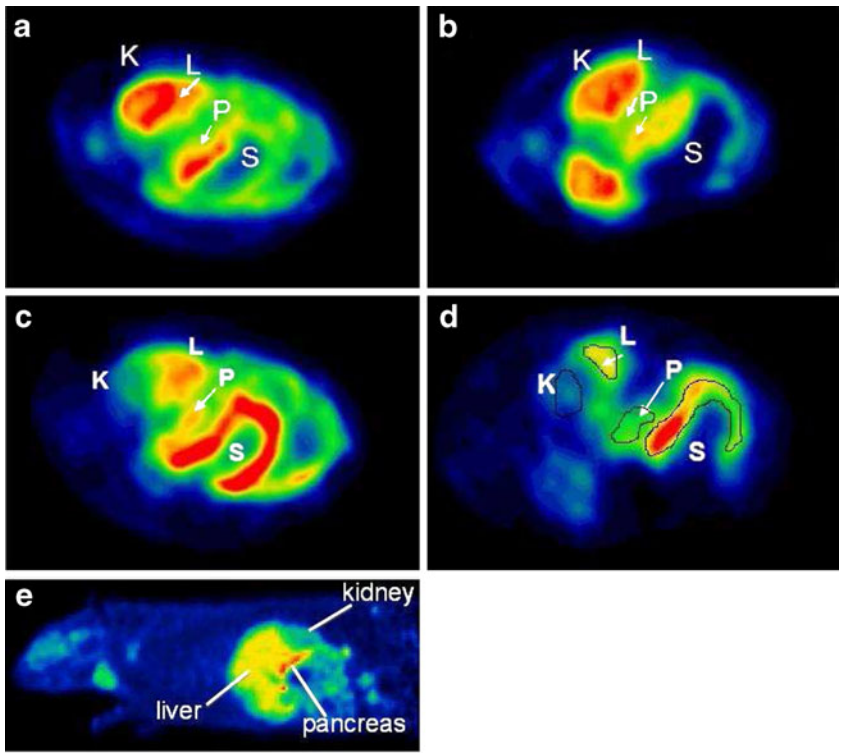

Fig. 1. PET images of transverse abdominal planes in S-D rats after a bolus tail-vein injection of [^{11}C]DTBZ. Early summed images (0–10 min postinjection) in **a** control S-D rats and **b** STZ-induced diabetic rats. Delayed images (60–90 min) showing difference between **c** control S-D rats and **d** STZ-induced diabetic rats (*K* kidney, *L* liver, *P* pancreas, *S* stomach). **e** Anatomical localization is seen in a representative sagittal image of a healthy S-D rat following injection of [^{18}F]FP-(+)-DTBZ.

stomach exhibited a slower, but continuous increase in uptake of the radiotracer. The differences in the TAC of the stomach and the pancreas were used to assist in the ROI definition in order to avoid contamination of signal by the stomach into the ROI of the pancreas. Specifically, an overlap of the pancreas ROI into the stomach region would be evidenced by a steady increase in the signal intensity, as opposed to the observed plateau and slow clearance of activity.

Imaging Pancreatic BCM with [^{11}C]DTBZ in Rodent Models of Obesity and Diabetes

In order to test the efficacy of targeting VMAT2 for imaging changes in pancreatic BCM in obesity and diabetes, we used three well-characterized rodent models: the STZ-treated rat with specific β-cell loss as a model of type 1 diabetes mellitus (DM), the Zucker diabetic fatty rat (ages 8, 12, and 16 weeks) as a model of type 2 diabetes, and the Zucker fatty rat (ages 8, 12, and 16 weeks) as a model of β-cell adaptation that compensates by increasing BCM and insulin secretion in the face of obesity-associated insulin resistance and does not develop diabetes.

On a group (S-D, STZ-S-D, ZF-8wk, ZF-12wk, ZF-16wk, ZDF-8wk, ZDF-12wk, ZDF-16wk) level, a positive correlation was observed between mean pancreatic SUV and mean insulin content and (Fig. 3a: R^2=0.436, p=0.04). Similarly, a highly significant correlation was obtained between mean percent insulin-positive BCM and mean pancreatic SUV (R^2=0.906, p=0.003) for the ZF and ZDF rats. However, inclusion of the data for the STZ-treated and untreated S-D rats weakened the correlation of pancreatic SUV with the insulin-positive BCM (Fig. 3b). The utility of [^{11}C]DTBZ to estimate BCM, however, varied considerably among the different rodent models (Table 1). We found that the best correlation of SUV (range 3.0–7.0) with either insulin content (range 8–131 ng/g liver) or insulin-positive islet area (range 0.24–0.71) was evident in the STZ model of type 1 diabetes. In the ZF rats, the change in SUV (range 3.1–6.1) relative to total insulin content (range 72–204 ng/g liver) was only about one third that seen in the STZ-treated and untreated rats. However, there was no positive correlation of SUV with the increase in insulin-positive islet area (range 1.39–8.03) with the obesity-associated adaptation of the β-cell function in the ZF rats. In the ZDF rats, we found no positive correlation of the pancreatic SUV (range 2.85–6.55) of [^{11}C]DTBZ SUV with either changes in insulin content (range 12–68 ng/g liver) or BCM (1.40–3.67). It is also worth noting that in cases where there were significant correlations, the y-intercept of these regression lines was not close to 0 and, for a given percent change in insulin content or islet area, the percent change in the SUV was substantially smaller.

We also evaluated the possibility of using the liver or kidney as reference regions, and that either the pancreas to

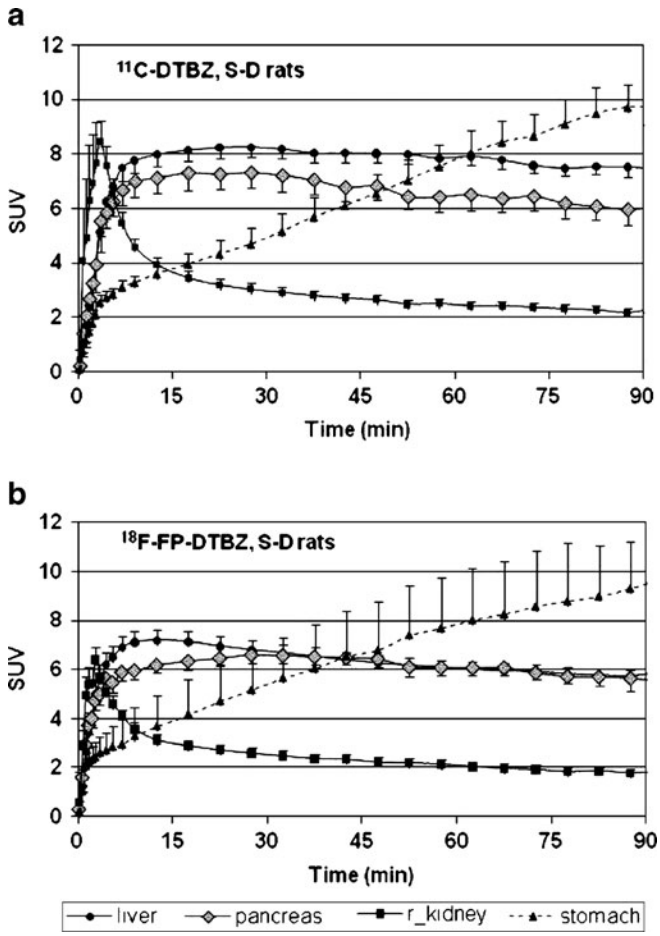

Fig. 2. Mean tissue time–activity curves expressed in SUV units in healthy S-D rats after a bolus injection of **a** [^{11}C]DTBZ (n=6) or **b** [^{18}F]FP-DTBZ (n=6).

liver (P/L), or the pancreas to kidney (P/K), ratios could serve as convenient indices of pancreatic [^{11}C]DTBZ uptake. The utility of the reference region is based on the premise that uptake of [^{11}C]DTBZ by either organ is nonspecific and does not vary with age or changes in body composition or other physiological factors associated with insulin resistance and diabetes. The reference region would be expected to provide a better normalization than SUV, in that it would more directly correct for differences in tracer clearance. We found that hepatic SUVs varied considerably within and between groups. While the correlations established on the basis of pancreatic SUVs were preserved for the P/L ratio in the STZ diabetic and ZF rats, the variation in the hepatic SUV in the ZDF rats was especially problematic. We observed a progressive decline in hepatic SUV with age in ZDF rats but minimal changes in pancreatic SUVs (Table 2). This led to spuriously higher P/L ratio values despite the lower pancreatic insulin content in older rats. The uptake and the absolute variability in the kidney cortex were less than that of hepatic SUV in agreement with previous reports [15, 16]. The steady-state signal in the kidney cortex most likely represents nonspecific binding, justifying its use as a reference region. However, diligence in the assignment of the ROIs is imperative, especially in longitudinal studies, as small errors in the quantification of the kidney SUV will translate into large errors in the P/K ratio. In conclusion, our results indicate that for [^{11}C]DTBZ quantitative imaging of BCM, the liver cannot be used as a reference region, but that with due diligence, the kidney cortex can serve as a reference region for quantification of pancreatic BCM across animal models of diabetes and β-cell hyperplasia.

Gastric [^{11}C]DTBZ Uptake

Apart from pancreatic [^{11}C]DTBZ measurements, we noted some trends in hepatic and gastric [^{11}C]DTBZ uptake. We

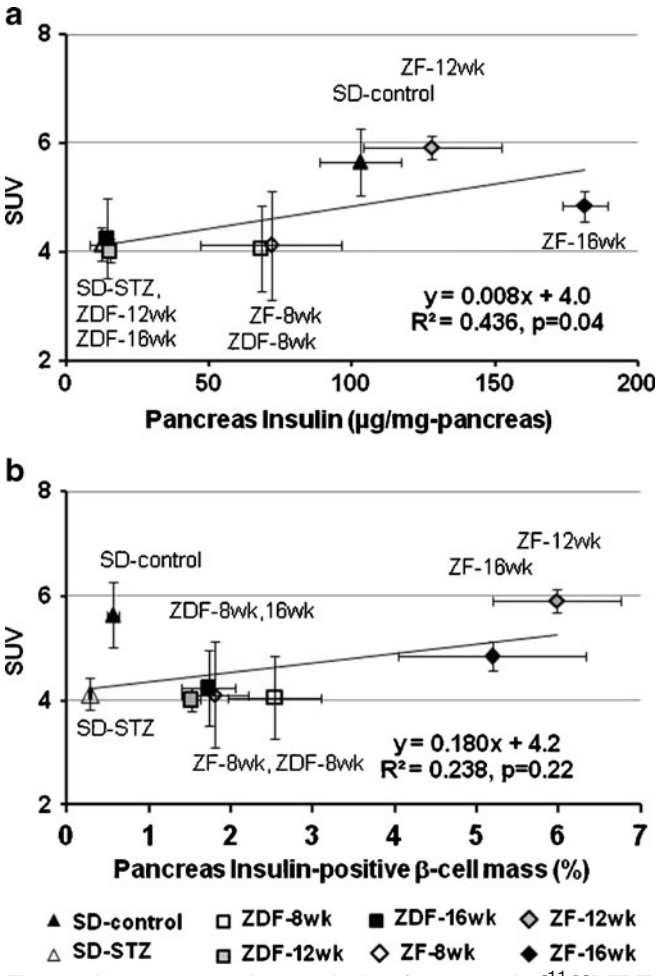

Fig. 3. Linear regression analysis of pancreatic [^{11}C]DTBZ SUV across rat models of diabetes and β-cell compensation. Data points are the mean pancreatic SUV from 60 to 90 min *vs.* **a** mean pancreatic insulin, or **b** mean fractional pancreatic insulin-positive β-cell area (S-D rats: *solid triangle* control (n=6), *open triangle* STZ-treated (n=5). ZDF rats: *open square* 8 weeks (n=4), *shaded square* 12 weeks (n=6), *solid square* 16 weeks (n=5). ZF rats: *open diamond* 8 weeks (n=5), *shaded diamond* 12 weeks (n=5), *solid diamond* 16 weeks (n=5)).

Table 1. Correlation of insulin content or insulin-positive islet area with pancreatic SUV of ^{11}C-DTBZ by PET imaging

Rat model	Pancreatic insulin content *vs.* pancreas SUV		Insulin-positive islet area *vs.* pancreas SUV	
STZ diabetic (T1DM)	$y=0.016x+4.0$	$R^2=0.320$, $p=0.088$	$y=4.39x+3.1$	$R^2=0.258$, $p=0.111$
ZF (β-cell hyperplasia)	$y=0.005x+4.2$	$R^2=0.090$, $p=0.513$	$y=-0.018x+4.9$	$R^2=0.002$, $p=0.934$
ZDF (T2DM)	$y=-0.024x+4.6$	$R^2=0.181$, $p=0.477$	$y=-0.240x+4.6$	$R^2=0.061$, $p=0.555$

noted a significant gastric uptake of [^{11}C]DTBZ, particularly on delayed images. Interestingly, the pattern of SUV changes across groups followed that of the pancreas, and a statistically significant correlation was obtained between mean gastric SUVs and mean insulin content ($R^2=0.694$, $p=0.01$) and percent beta-cell values ($R^2=0.687$, $p=0.01$). STZ is known to induce enterochromaffin cell damage, perhaps explaining the significant decline in gastric VMAT2 signal in STZ rats [30]. Similarly, a generalized weight increase in ZF rats could account for the patterns observed in these rat groups. We noticed a significantly higher concentration of [^{11}C]DTBZ along the lesser curvature of the stomach which incidentally receives the majority of autonomic innervation through the nerve of Latarjet [31]. Further studies may be warranted to study the role of DTBZ in gastric imaging, particularly in conditions like diabetic gastopathy.

Comparison of [^{11}C]DTBZ and [^{18}F]FP-(+)-DTBZ Uptake in STZ-Induced Diabetes

Pancreatic SUV of both [^{11}C]DTBZ and [^{18}F]FP-(+)-DTBZ was observed to decrease in tandem with the progressive loss of pancreatic insulin content (Fig. 4a, b) and of insulin-positive BCM (Fig. 4c, d). The ~2-fold increase in the slope of SUV with change in insulin content of [^{18}F]FP-(+)-DTBZ compared to [^{11}C]DTBZ ($p=0.153$) is consistent with the reported increased affinity of [^{18}F]FP-(+)-DTBZ [22]. However, similar background activity remained in the diabetic STZ-treated rats for both [^{11}C]DTBZ and [^{18}F]FP-(+)-DTBZ. It should be noted that the imaging session post-STZ treatment for the [^{11}C]DTBZ imaging was 120 h, compared to 13–96 h for the [^{18}F]FP-(+)-DTBZ imaging. It is conceivable that factors other than β-cell loss may impact upon VMAT2 expression following STZ treatment and may confound the comparison between the two imaging agent. Using a more limited data set of the nontreated ($n=9$) and the 96-h post-STZ treatment ($n=3$) rats, the slope of [^{18}F]FP-(+)-DTBZ SUV with insulin content was somewhat reduced, but remained 1.6-fold higher than the corresponding slope for [^{11}C]DTBZ. The intercept, representing background binding, did not change.

Our HPLC analysis for [^{18}F]FP-(+)-DTBZ and its metabolites confirmed that between 60- and 90-min radioactivity in the pancreas was attributable almost exclusively to [^{18}F]FP-(+)-DTBZ (%parent: pancreas 97±0.3, liver 87±1, kidney 82±2, plasma 71±2).

Specific and Nonspecific Uptake of FP-(+)-DTBZ

At $t=90$ min following the start of the [^{18}F]FP-(+)-DTBZ imaging sessions, a subset of the rats (controls: $n=9$, STZ diabetic: $n=6$) shown in Figs. 2b and 4b, d received a displacing dose of unlabeled FP-(+)-DTBZ (2.5 mg/kg) to assess specific and nonspecific uptake of the radiotracer. The displacing dose of unlabeled FP-(+)-DTBZ was ~5,500-fold greater than the mass dose of [^{18}F]FP-(+)-DTBZ (FP-(+)-DTBZ—2.5 mg/kg, [^{18}F]FP-(+)-DTBZ—4.6×10^{-4} mg/kg), a dose that can be assumed to be sufficient to displace all specifically bound radioligands. In the control rats, the unlabeled FP-(+)-DTBZ had no discernable effect on liver or kidney activity, but displaced ~60% of the bound activity from the pancreas and ~80% from the stomach (Fig. 5a). In the STZ-treated rats, a smaller but clearly detectable displacement of activity was observed in both the stomach and the pancreas, despite minimal residual insulin content or insulin-positive cell mass (Fig. 5b).

Assuming that the ~5,500-fold excess dose of unlabeled FP-(+)-DTBZ given is sufficient to displace specifically bound radiotracer, these results indicate the existence of two components of FP-(+)-DTBZ uptake. One component is

Table 2. Mean standardized uptake values of ^{11}C-DTBZ (60–90 min)

	STZ diabetic (T1DM)		ZF (β-cell hyperplasia)			ZDF (T2DM)		
	Control	STZ	8 weeks	12 weeks	16 weeks	8 weeks	12 weeks	16 weeks
Pancreas	5.7±0.6	4.1±0.3	4.1±1.0	5.9±0.2	4.9±0.3	4.1±0.8	4.0±0.2	4.3±0.7
Liver	7.6±0.1	7.5±0.04	7.4±0.1	8.8±0.2	6.2±0.05	6.8±0.7	5.8±0.1	4.9±0.1
Kidney	2.4±0.03	1.8±0.02	1.4±0.04	2.3±0.1	2.2±0.03	2.0±0.05	1.9±0.02	1.8±0.03

Values are mean ± SEM

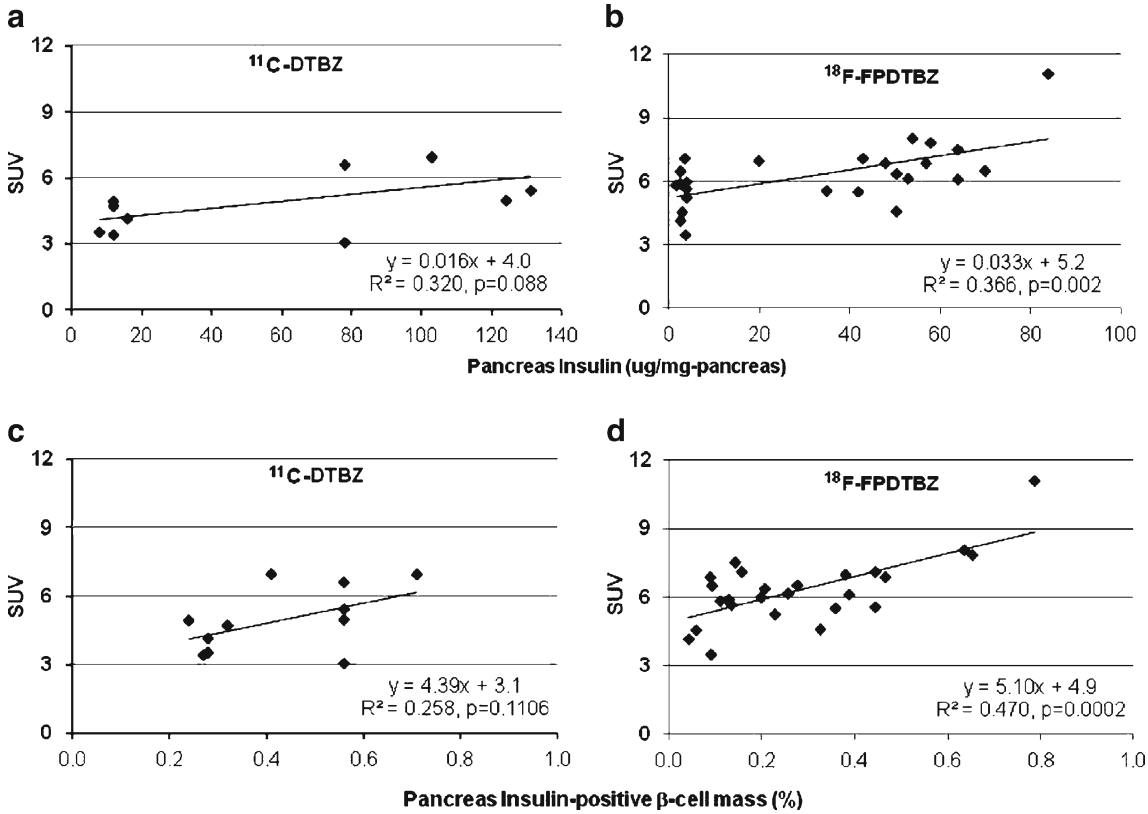

Fig. 4. Linear regression analysis of pancreatic standardized uptake values (*SUV*) in healthy and STZ-treated S-D rats *vs*. mean pancreatic insulin (**a**, **b**), or mean fractional pancreatic insulin-positive β-cell area (**c**, **d**). Mean SUVs from 60 to 90 min after a bolus injection of [^{11}C]DTBZ (**a**, **c**) or [^{18}F]FP-DTBZ (**b**, **d**). All STZ-treated rats injected with [^{11}C]DTBZ were imaged 120 h post-STZ treatment. For the [^{18}F]FP-DTBZ studies, imaging time post-STZ varied from 13 to 96 h in order to provide intermediate points of insulin content.

nondisplaceable and nonspecific within the liver, kidney, stomach, and pancreas and is represented by the [^{18}F]FP-(+)-DTBZ SUV following displacement with unlabeled FP-(+)-DTBZ. The difference between [^{18}F]FP-(+)-DTBZ SUV before (60–90 min) and after (150–180 min) displacement with FP-(+)-DTBZ represents specific uptake within the stomach and pancreas. If the specific pool of FP-(+)-DTBZ in the pancreas represents VMAT2-positive cells, primarily neuro-tissue and β cells [18, 32], then one would predict that this displaceable uptake would be proportional to insulin-positive pancreatic β-cell mass. As shown in Fig. 6, both the total (Fig. 6a: specific and nonspecific uptake) and the displaceable (Fig. 6b: specific uptake) pancreatic SUV correlated with pancreatic insulin. The mean nonspecific pancreatic SUV was the same in both the control and STZ diabetic rats (control 2.7±0.2, STZ diabetic 2.5±0.3), whereas there was a 35% reduction (p=0.037) in the specific uptake in the STZ diabetic rats compared to the controls (Fig. 6c). Thus, we estimate that 61±2% of [^{18}F]FP-(+)-DTBZ uptake is specific, and assuming negligible β cells in the STZ diabetic animals, that β cells represent ~35% of the specific uptake within the pancreas of healthy nondiabetic rats, or ~25% of the total pancreatic uptake. The presence of a substantial fraction of [^{18}F]FP-(+)-DTBZ and [^{11}C]DTBZ not bound to BCM is consistent with the magnitude of the intercept of the linear regression analyses (Figs. 3, 4, and 6).

Discussion

This is the first study to evaluate [^{11}C]DTBZ for BCM imaging across rat models of diabetes and pre-diabetic conditions encompassing type 1 diabetes, type 2 diabetes, and nondiabetic β-cell hyperplasia and to directly compare the efficacy of BCM imaging with [^{11}C]DTBZ *vs*. [^{18}F]FP-(+)-DTBZ, which are currently the best available imaging agents of BCM. The underlying strategy for imaging of pancreatic BCM with either [^{11}C]DTBZ or [^{18}F]FP-(+)-DTBZ is the specific uptake of these radiotracers into the insulin secretory granules of the β cell mediated by VMAT2. It should be noted though that possible differences across rat strains of the association of VMAT2 levels with insulin content per β cell are not known and may impact the correlation of pancreatic uptake of DTBZ analogs with β-cell mass and its associated insulin content. Nevertheless, we observed an excellent correlation between pancreatic [^{18}F]FP-(+)-DTBZ uptake as measured by pancreatic SUV and the indices of insulin content and percent β-cell area in the STZ model of type 1 diabetes and of [^{11}C]DTBZ across the

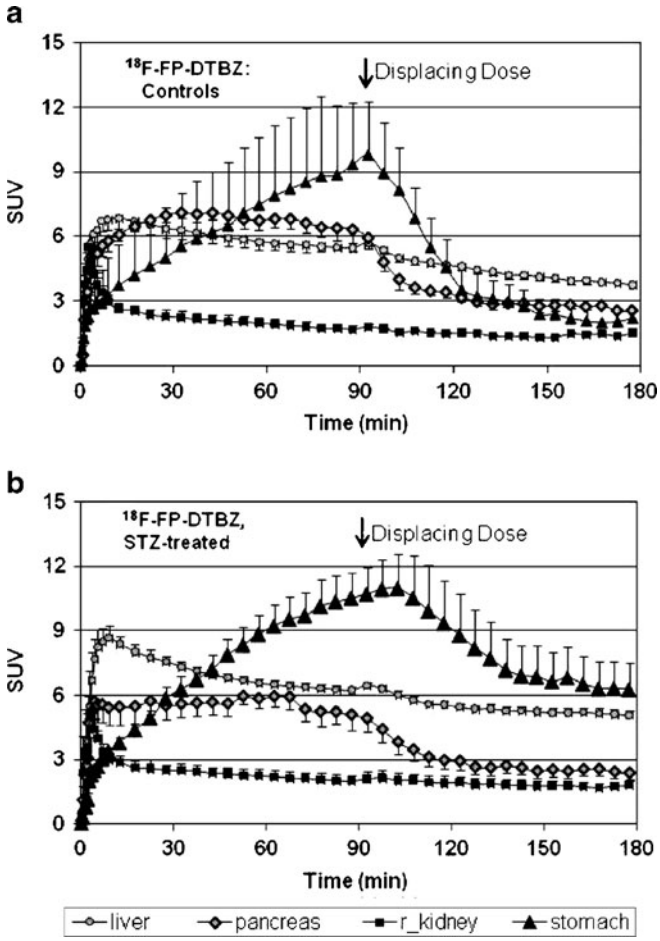

Fig. 5. Mean tissue time–activity curves in SUV units in **a** healthy ($n=5$) and **b** STZ diabetic ($n=6$) S-D rats after a bolus injection of [^{18}F]FP-DTBZ given at $t=0$ min. At $t=90$ min, a displacing dose of unlabeled FP-DTBZ (2.5 mg/kg rat) was administered as a bolus injection. Rats shown here are a subset of those included in Figs. 2b and 4b, d.

models of type 1 and type 2 diabetes and compensatory hyperplasia covering a ~10-fold range in BCM.

The results presented in this paper are based on total uptake of radiotracer in pancreas as measured by SUV. Although SUV is normalized by injected dose and body weight, a metric that quantitatively accounts for the availability of tracer (*e.g.*, in plasma or a reference tissue lacking specific binding) would be a theoretically more accurate outcome. Previous studies investigating beta-cell mass with VMAT2 radioligands have used the renal cortex as a reference region and the results of our displacement experiments suggested that the kidney lacks specific binding [13, 15, 18]. We therefore analyzed the pancreas TACs by applying the multilinear reference tissue model using kidney data as input functions to estimate binding potential (BP_{ND}), the ratio of specifically bound tracer to nondisplaceable concentration at equilibrium [33]. BP_{ND} measurements from [^{11}C]DTBZ and [^{18}F]FP-(+)-DTBZ data correlated positively with pancreas insulin content ($R^2=0.29$ for [^{11}C]DTBZ and 0.26 for [^{18}F]FP-(+)-DTBZ), but less strongly than did pancreas SUV against insulin ($R^2=0.32$ for [^{11}C]DTBZ and 0.37 for [^{18}F]FP-(+)-DTBZ). As noted in the "Results", variability in the assignment of regions on the renal cortex and time-varying partial volume effects associated with imaging such a thin structure are likely sources of error, which may have added variability to the BP_{ND} estimates. Fortunately, we anticipate that these factors will be less significant in human studies, due to a better match of structure size and spatial resolution.

Prior to the onset of type 2 diabetes, obesity often leads to peripheral insulin resistance. However, compensation by an enhanced insulin secretory response by the β cell can maintain normoglycemic levels and minimize abnormal postpandrial glycemia. In part, increases in BCM can account for the hypersecretory response. In fact, type 2 DM is characterized by an *increase* in BCM with time in response to peripheral insulin resistance. Indeed, type 2 DM is often associated with the "metabolic syndrome" characterized by obesity and hyperlipidemia. ZF rats serve as a model of obesity and have demonstrated an increase in BCM with age and weight [34]. With the increase in body fat mass of the ZF rat from 8 to 16 weeks, the changes in pancreatic β cell were most evident in the increase in BCM, rather than pancreatic insulin. During this 8-week time period, BCM increased by ~2.6-fold and insulin by ~1.7-fold. In an earlier study of β-cell adaptation in ZF rats, Liu *et al.* also found a modest 1.3-fold increase in the insulin content of 12-week ZF rats compared to 12-week Zucker lean rats, despite the 3.8-fold increase in BCM [26]. An even greater disparity is observed in a comparison of the S-D and ZF rats in our study, where the 9.3-fold increase in BCM is associated only with a 1.5-fold increase in insulin content. These results indicate a marked decrease in the insulin content per β cell in the ZF rats with the development of obesity. The positive correlation of the pancreatic SUV of the PET image with insulin content but not with BCM in the ZF rat is consistent with an increase in the number of insulin secretory granules together with increased VMAT2 protein.

As a model of type 2 diabetes, ZDF rats exhibit a loss of glucose-stimulated insulin secretion prior to the loss of beta-cell mass [35]. The ZDF diabetic variant of the Zucker fatty rat colony [36] is a model for prediabetes and type 2 DM as they manifest an increase in BCM till 18 weeks of age, followed by a progressive loss of β cells [34, 36]. Despite this increase in BCM, ZDF rats manifest a progressive loss of insulin production from 10 weeks of age [37]. In our study, there was significantly lower insulin content in 12- and 16-week-old ZDF rats whereas the percent beta-cell area remained unchanged. Indeed, we did not notice a change in [^{11}C]DTBZ SUV in ZDF rats over age consistent with the percent β-cell area changes. These results suggest that a constant number of insulin secretory vesicles as diabetes develops in the ZDF rat, but that an overall depletion of insulin content within the vesicles occurs. As a diagnostic tool, PET imaging of [^{11}C]DTBZ uptake in the pancreas may be useful for identifying those type 2 diabetic patients

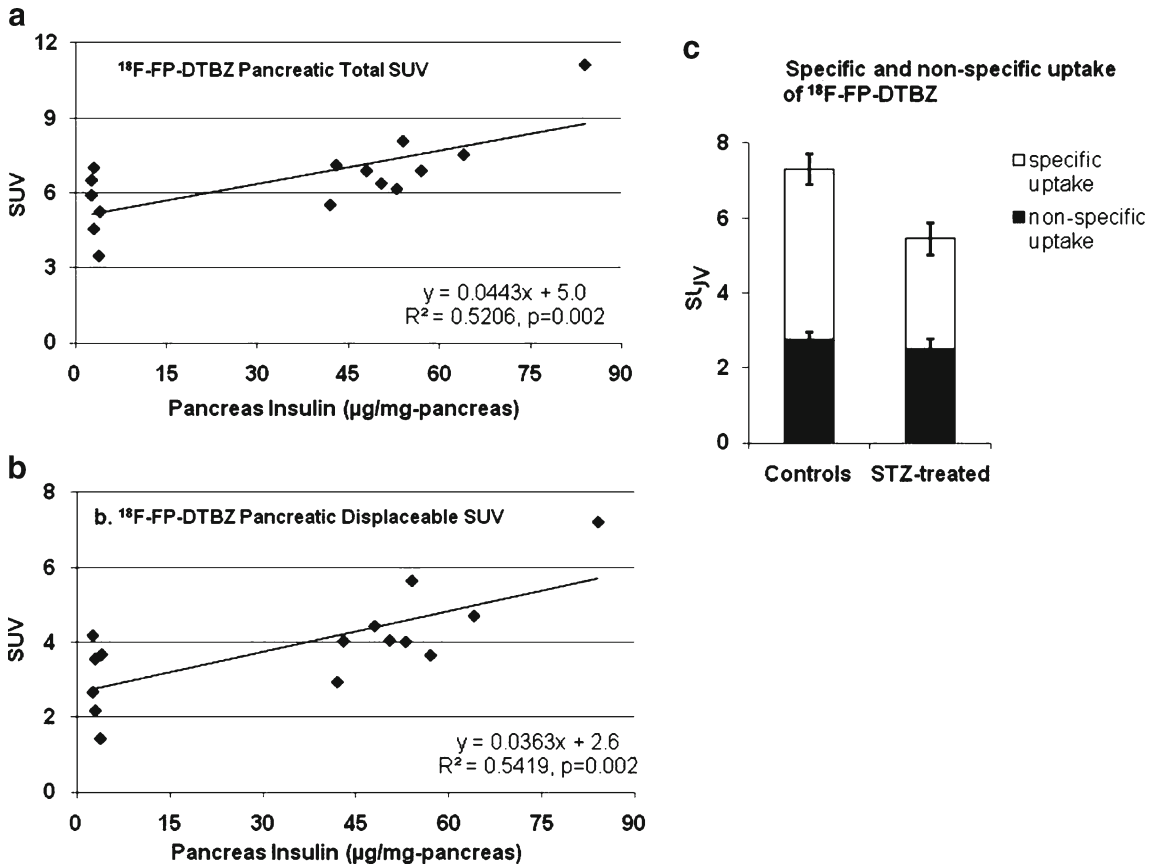

Fig. 6. Linear regression analysis of **a** total and **b** displaceable pancreatic SUV in healthy and STZ-treated S-D rats *vs*. mean pancreatic insulin. Total pancreatic SUV is the mean from 60 to 90 min after a bolus injection of [^{18}F]FP-DTBZ. Displaceable pancreatic SUV was calculated as the difference between the total pancreatic SUV and pancreatic SUV 60–90 min after a displacing dose of unlabeled FP-DTBZ (2.5 mg/kg rat), as shown in Fig. 5. **c** Specific uptake of [^{18}F]FP-DTBZ was calculated as the fraction of displaceable [^{18}F]FP-DTBZ. Nonspecific uptake was calculated as the pancreatic SUV remaining 60–90 min after a displacing dose of unlabeled FP-DTBZ. Rats shown here are a subset of those included in Figs. 2b and 4b, d.

that have reduced β-cell function despite intact BCM and guide the design of therapies to restore islet function.

STZ-induced diabetes in experimental animals serves as a model of type 1 diabetes with the selective loss of beta-cell mass. Compared to their healthy controls, we have noted a ~30% reduction of both the [^{11}C]DTBZ and the [^{18}F]FP-(+)-DTBZ SUV in STZ-treated rats, whereas Souza *et al.* observed a 65% reduction in an alternative rat model of type 1 diabetes (BB-DP) [16]. A possible explanation for this difference may be accounted for by the distribution of VMAT2 in pancreatic islet innervations. It is known that VMAT2 is present on both sympathetic neurons and beta cells in pancreas [19]. The concentration of VMAT2 in pancreatic sympathetic neurons is higher than in beta cells and can be distinguished based on appearance on immunohistochemical examination [19]. The [^{11}C]DTBZ and [^{18}F]FP-(+)-DTBZ PET signal is a sum total of the DTBZ bound to VMAT2 on both sympathetic neurons and beta cells. It has been reported that STZ does not damage VMAT2 on sympathetic nerves [38] but does damage VMAT2 in beta cells [39]. Eight-fold reductions in VMAT2 transcript concentration were noted in beta cells following STZ treatments [39]. On the other hand, there is a progressive damage to sympathetic nerves along with beta cells in BB-DP models [38]. A combined damage to both sources of VMAT2 may be responsible for the lower pancreatic binding of DTBZ in BB-DP rats as compared to STZ-treated rats where only the VMAT2 in beta cells is damaged.

The displacement of ~60% of pancreatic [^{18}F]FP-(+)-DTBZ with unlabeled FP-(+)-DTBZ in our rats was similar to that seen with either pretreatment or coinjection of the unlabeled compound [12]. This displaceable pool of radioligand has been interpreted to represent FP-(+)-DTBZ binding sites on VMAT2. Not previously reported though, the fraction of displaceable [^{18}F]FP-(+)-DTBZ was dependent upon BCM, supporting the hypothesis that this represents VMAT2 binding sites within the pancreatic β cells. However, even in those rats with little residual pancreatic insulin or BCM, a substantial pool of displaceable and hence specifically bound radioligand remained in the pancreas. From a comparison of the healthy S-D rats and the STZ-treated rats, we estimate that ~65% of the specifically bound [^{18}F]FP-(+)-DTBZ is binding to VMAT2 (or another saturable site) that is not associated with insulin-positive β

cells. When also including the nonspecifically bound tracer, we estimate that ~25% of the total uptake can be attributed to β-cell uptake. In addition to the probability that sympathetic nerves within the pancreas contribute to the pool of reversible binding sites, Saisho *et al.* also identified VMAT2-positive pancreatic polypeptide (PP) cells within the pancreatic islet [32]. In our STZ-treated animals, the toxicity is limited largely to the β cell, leaving the PP cells unaffected [40, 41]. Thus, the contribution of PP cells to the reversibly bound radioligand pool may be significant in our studies, as well as in the PET imaging of humans. PP cells have been shown to constitute up to ~2% of the volume density in the head of the pancreas in healthy controls, as well as type 1 and type 2 diabetic patients [42], and may have contributed to the [^{11}C]DTBZ specifically bound background signal present in the pancreas of C-peptide-negative type 1 diabetic patients [17].

Conclusion

Our study confirms the finding of significant reduction of DTBZ and FP-DTBZ uptake in STZ diabetic rats as compared to healthy S-D rats besides demonstrating for the first time the correlation between DTBZ uptake across a wide spectrum of disease including evolving type 2 diabetes mellitus and nondiabetic beta-cell hyperplasia in animal models. While a substantial fraction of binding to VMAT2 in β cells is clear, there is also significant specific and nonspecific binding of these VMAT2-targeted radioligands which may limit the quantification of physiologically relevant changes in BCM. However, despite these limitations, our results suggest that [^{18}F]FP-(+)-DTBZ can be used to noninvasively and quantitatively image insulin-positive BCM in type 1 diabetic patients. Thus, [^{18}F]FP-(+)-DTBZ may prove valuable as a diagnostic tool in assessing treatments to improve functional BCM in type 1 and type 2 diabetes.

Acknowledgments. The authors acknowledge the excellent work of the staff of the Yale PET Center and Tim Mulnix, PhD for the rat holder and technical assistance critical to the success of these studies. These studies were supported by the Yale-Pfizer Bioimaging Alliance and the Juvenile Diabetes Research Foundation (1 37-2009-29). This publication was also made possible by CTSA Grant Number UL1 RR024139 from the National Center for Research Resources (NCRR), a component of the National Institutes of Health (NIH), and NIH roadmap for Medical Research. Its contents are solely the responsibility of the authors and do not necessarily represent the official view of NCRR or NIH.

Conflicts of Interest/Disclosures. Walter C. Soeller owns shares in Pfizer, Inc. and Judith L. Treadway is an employee and shareholder of Pfizer, Inc.

References

1. Finegood DT, McArthur MD, Kojwang D et al (2001) Beta-cell mass dynamics in Zucker diabetic fatty rats. Rosiglitazone prevents the rise in net cell death. Diabetes 50:1021–1029
2. Medarova Z, Evgenov NV, Dai G, Bonner-Weir S, Moore A (2006) *In vivo* multimodal imaging of transplanted pancreatic islets. Nat Protoc 1:429–435
3. Saudek F, Brogren CH, Manohar S (2008) Imaging the beta-cell mass: why and how. Rev Diab Stud RDS 5:6–12
4. Harris PE, Ferrara C, Barba P, Polito T, Freeby M, Maffei A (2008) VMAT2 gene expression and function as it applies to imaging beta-cell mass. J Molecul Med 86:5–16
5. Robertson RP (2007) Estimation of beta-cell mass by metabolic tests: necessary, but how sufficient? Diabetes 56:2420–2424
6. Evgenov NV, Medarova Z, Dai G, Bonner-Weir S, Moore A (2006) *In vivo* imaging of islet transplantation. Nat Med 12:144–148
7. Antkowiak PF, Tersey SA, Carter JD, Vandsburger MH, Nadler JL, Epstein FH, Mirmira RG (2009) Noninvasive assessment of pancreatic beta-cell function *in vivo* with manganese-enhanced magnetic resonance imaging. Am J Physiol Endocrin Metab 296:E573–E578
8. Schmitz A, Shiue CY, Feng Q et al (2004) Synthesis and evaluation of fluorine-18 labeled glyburide analogs as beta-cell imaging agents. Nucl Med Biol 31:483–491
9. Schneider S, Feilen PJ, Schreckenberger M et al (2005) *In vitro* and *in vivo* evaluation of novel glibenclamide derivatives as imaging agents for the non-invasive assessment of the pancreatic islet cell mass in animals and humans. Exp Clin Endocrinol Diab 113:388–395
10. Wangler B, Beck C, Shiue CY et al (2004) Synthesis and *in vitro* evaluation of (S)-2-([I11C]methoxy)-4-[3-methyl-1-(2-piperidine-1-yl-phenyl)-butyl-carbamoyl]-benzoic acid ([11C]methoxy-repaglinide): a potential beta-cell imaging agent. Bioorg Med Chem Lett 14:5205–5209
11. Wangler B, Schneider S, Thews O et al (2004) Synthesis and evaluation of (*S*)-2-(2-[18F]fluoroethoxy)-4-([3-methyl-1-(2-piperidin-1-yl-phenyl)-butyl-carbamoyl]-methyl)-benzoic acid ([18F]repaglinide): a promising radioligand for quantification of pancreatic beta-cell mass with positron emission tomography (PET). Nucl Med Biol 31:639–647
12. Kung HF, Lieberman BP, Zhuang Z-P et al (2008) *In vivo* imaging of vesicular monoamine transporter 2 in pancreas using an 18F epoxide derivative of tetrabenazine. Nucl Med Biol 35:825–837
13. Kung M-P, Hou C, Lieberman BP et al (2008) *In vivo* imaging of β-cell mass in rats using 18F-FP-(+)-DTBZ: a potential PET ligand for studying diabetes mellitus. J Nucl Med 49:1171–1176
14. Harris PE, Ferrara C, Barba P, Polito T, Freeby M, Maffei A (2008) VMAT2 gene expression and function as it applies to imaging beta-cell mass. J Molec Med 86:5–16
15. Simpson NR, Souza F, Witkowski P et al (2006) Visualizing pancreatic β-cell mass with [11C]DTBZ. Nuc Med Biol 33:855–864
16. Souza F, Simpson N, Raffo A et al (2006) Longitudinal noninvasive PET-based β-cell mass estimates in a spontaneous diabetes rat model. J Clin Invest 116:1506–1513
17. Goland R, Freeby M, Parsey R et al (2009) 11C-Dihydrotetrabenazine PET of the pancreas in subjects with long-standing type 1 diabetes and in healthy controls. J Nucl Med 50:382–389
18. Weihe E, Eiden LE (2000) Chemical neuroanatomy of the vesicular amine transporters. FASEB J 14:2435–2449
19. Anlauf MR, Eissele MK, Schafer LE et al (2003) Expression of the two isoforms of the vesicular monoamine transporter (VMAT1 and VMAT2) in the endocrine pancreas and pancreatic endocrine tumors. J Histochem Cytochem 51:1027–1040
20. Maffei AZ, Liu P, Witkowski F et al (2004) Identification of tissue-restricted transcripts in human islets. Endocrin 145:4513–4521
21. Weihe E, Schafer MK, Erickson JD, Eiden LE (1994) Localization of vesicular monoamine transporter isoforms (VMAT1 and VMAT2) to endocrine cells and neurons in rat. J Molec Neurosci MN 5:149–164
22. Kung MP, Hou C, Goswami R, Ponde DE, Kilbourn MR, Kung HF (2007) Characterization of optically resolved 9-fluoropropyl-dihydrotetrabenazine as a potential PET imaging agent targeting vesicular monoamine transporters. Nucl Med Biol 34:239–246
23. Kilbourn MR, Hockleya B, Leea L et al (2007) Pharmacokinetics of [18F]fluoroalkyl derivatives of dihydrotetrabenazine in rat and monkey brain. Nuc Med Biol 34:233–237
24. Larsen P, Ulin J, Dahlstrom K, Jensen M (1997) Synthesis of [11C] iodomethane by iodination of [11C]methane. Appl Radiat Isot 48:153–157
25. Jewett D (1992) A simple synthesis of [11C]methyl triflate. Appl Radiat Isot 43:1383–1385
26. Liu YQ, Jetton TL, Leahy JL (2002) β-Cell adaptation to insulin resistance. J Biol Chem 277:39163–39168
27. Pick A, Kubstrub CJ, Levisetti M, Pugh W, Bonner-Weir S, Polonsky KS (1998) Role of apoptosis in failure of beta-cell mass compensation for insulin resistance and beta-cell defects in the Zucker diabetic fatty rat. Diabetes 47:358–364

28. Carson RE, Barker WC, Liow JS, Johnson CA (2003) Design of a motion-compensation OSEM list-mode algorithm for resolution-recovery reconstruction for the HRRT. IEEE Nucl Sci Symp Conf Rec 5:3281–3285
29. Rasband WS. Image J. U. S. National Institutes of Health, Bethesda, Maryland, USA, http://rsb.info.nih.gov/ij/, 1997–2009
30. Brenna O, Qvigstad G, Brenna E, Waldum HL (2003) Cytotoxicity of streptozotocin on neuroendocrine cells of the pancreas and the gut. Dig Dis Sci 48:906–910
31. Takahashi T, Kantoh M, Kusunoki M, Yamamura T, Utsunomiya J (1989) Different innervation mechanisms between the lesser and greater curvature of guinea pig antrum. Dig Dis Sci 34:220–224
32. Saisho Y, Harris PE, Butler AE, Galasso R, Gurlo T, Rizza RA, Butler PC (2008) Relationship between pancreatic vesicular monoamine transporter 2 (VMAT2) and insulin expression in human pancreas. J Mol Hist 39:543–551
33. Ichise M, Liow JS et al (2003) Linearized reference tissue parametricimaging methods: application to [11C]DASB positron emission tomographystudies of the serotonin transporter in human brain. J Cereb Blood FlowMetab 23:1096–1112
34. Bray GA (1977) The Zucker-fatty rat: a review. Fed Proc 36:148–153
35. Ohneda M, Inman LR, Unger RH (1995) Caloric restriction in obese pre-diabetic rats prevents beta-cell depletion, loss of beta-cell GLUT 2 and glucose incompetence. Diabetologia 38:173–179
36. Clark JB, Palmer CJ, Shaw WN (1983) The diabetic Zucker fatty rat. Proc Soc Exp Biol Med 173:68–75
37. Janssen SW, Hermus AR, Lange WP (2001) Progressive histopathological changes in pancreatic islets of Zucker diabetic fatty rats. Exp Clinic Endoc Diab 109:273–282
38. Mei Q, Mundinger TO, Lernmark A, Taborsky GJ Jr (2002) Early, selective, and marked loss of sympathetic nerves from the islets of BioBreeder diabetic rats. Diabetes 51:2997–3002
39. Raffo A, Hancock K, Polito T et al (2008) Role of vesicular monoamine transporter type 2 in rodent insulin secretion and glucose metabolism revealed by its specific antagonist tetrabenazine. J Endocrin 198:41–49
40. Lenzen S (2008) The mechanism of alloxan- and streptozotocin-induced diabetes. Diabetologia 51:216–226
41. Sundler F, Hakason R, Lundquist I, Larsson L-I (1977) Effect of alloxan on pancreatic polypeptide (PP) cells. Cell Tissue Res 178:307–312
42. Rahier J, Wallon J, Loozen A, Lefevre W, Gepts W, Hao J (1983) The pancreatic polypeptide cells in the human pancreas: the effects of age and diabetes. J Clin Endocrinol Metab 56:441–444